

Regulating the Interlayer Spacings of Hard Carbon Nanofibers Enables Enhanced Pore Filling Sodium Storage

Congcong Cai, Yongan Chen, Ping Hu, Ting Zhu, Xinyuan Li, Qiang Yu, Liang Zhou,*
Xiaoyu Yang, and Liqiang Mai*

Hard carbon (HC) represents an attractive anode material for sodium-ion batteries. However, most HC materials deliver limited capacity and the sodium storage mechanisms in the slope and plateau regions are controversial. Herein, a series of hard carbon nanofibers (HCNFs) with tunable interlayer spacings are designed to understand the sodium storage manners in HC. The optimized HCNFs featuring short-range graphitic layers with sufficient interlayer spacings (0.37–0.40 nm) for Na⁺ intercalation deliver a high reversible capacity (388 mAh g⁻¹ at 30 mA g⁻¹) and good rate capability. In-situ X-ray diffraction and Raman characterizations reveal a revised adsorption/insertion–filling sodium storage mechanism. Combined with the density functional theory (DFT) calculation, the detailed relationship between pore-filling plateau capacity and interlayer spacing is disclosed. It is found that sufficient interlayer spacings (>0.37 nm) provide diffusion channels for Na⁺ to reach the pores for further filling. Additionally, the reason for plateau-region capacity degradation of the HCNFs is completely demonstrated. This contribution provides insights into the sodium storage mechanism and rational construction of high-performance HC anode materials.

1. Introduction

Sodium-ion batteries (SIBs) are promising alternatives to lithium-ion batteries (LIBs) due to the abundant and low-cost sodium resources.^[1–3] However, graphite, the commercial LIB anode material, can't work in SIBs, mainly because its Na-graphite compounds are not thermodynamically stable, and thus the insertion of sodium ions into graphite is not a spontaneous process.^[4] Although a number of anode materials, such as metal oxides/sulfides^[5–7] and alloys^[8–10] have been reported

for SIBs, many of them face either cost or environmental pollution issues, hindering the practical applications. In contrast, low-cost and environment-friendly carbonaceous materials are extremely attractive for industrial applications.

Hard carbon (HC) materials have demonstrated superior sodium storage performance for their large interlayer spacing (> 0.34 nm) and low operation potential (<0.3 V vs. Na⁺/Na).^[11,12] The irregularly arranged graphitic layers of HC are able to provide rich sodium storage sites.^[13,14] HC materials are generally prepared by pyrolyzing various precursors, such as carbohydrates,^[15,16] biomass wastes,^[17–20] and polymers.^[21–24] However, the capacity of these HC materials is relatively low, usually below 350 mAh g⁻¹. Many efforts have been made on creating more active sites by nanostructure design,^[25–28] porous structure construction,^[29,30] and heteroatom doping^[31–35] to further increase the capacity. Besides, the sodium storage mechanisms of HC in the slope (>0.1 V) and plateau (<0.1 V) regions are still in controversy.^[36–38] For example, Hu et al. designed multi-shelled hollow carbon nanospheres and proposed an adsorption–filling mechanism, corresponding to the sodium storage manners in the slope and plateau regions.^[39] Xiao et al. prepared low-defect and low-porosity carbon nanospheres and proposed an adsorption–insertion charge storage mechanism.^[40] Despite these advances, designing high-performance HC materials and understanding their sodium storage mechanism are still of significant importance.

Herein, we constructed a series of porous and robust hard carbon nanofibers (HCNFs) with tunable interlayer spacings by precisely adjusting the carbonization temperature. The HCNFs with abundant short-range graphitic layers and optimized interlayer spacings of 0.37–0.40 nm demonstrate a high reversible capacity (388 mAh g⁻¹ at 30 mA g⁻¹) and good rate performance (167 mAh g⁻¹ at 500 mA g⁻¹). In-situ X-ray diffraction (XRD) and Raman measurements reveal a revised adsorption/insertion–filling sodium storage mechanism for the HCNFs. In addition, combined with the density functional theory (DFT) calculations, the relationship between slope- and plateau-region capacities is disclosed and the reason for capacity degradation is demonstrated.

C. C. Cai, Y. A. Chen, P. Hu, T. Zhu, X. Y. Li, Q. Yu, L. Zhou, X. Y. Yang, L. Q. Mai
State Key Laboratory of Advanced Technology for Materials Synthesis and Processing
Wuhan University of Technology
Wuhan 430070, P. R. China
E-mail: liangzhou@whut.edu.cn; mlq518@whut.edu.cn
P. Hu, L. Zhou, L. Q. Mai
Foshan Xianhu Laboratory of the Advanced Energy Science and Technology Guangdong Laboratory
Foshan 528200, China

 The ORCID identification number(s) for the author(s) of this article can be found under <https://doi.org/10.1002/smll.202105303>.

DOI: 10.1002/smll.202105303

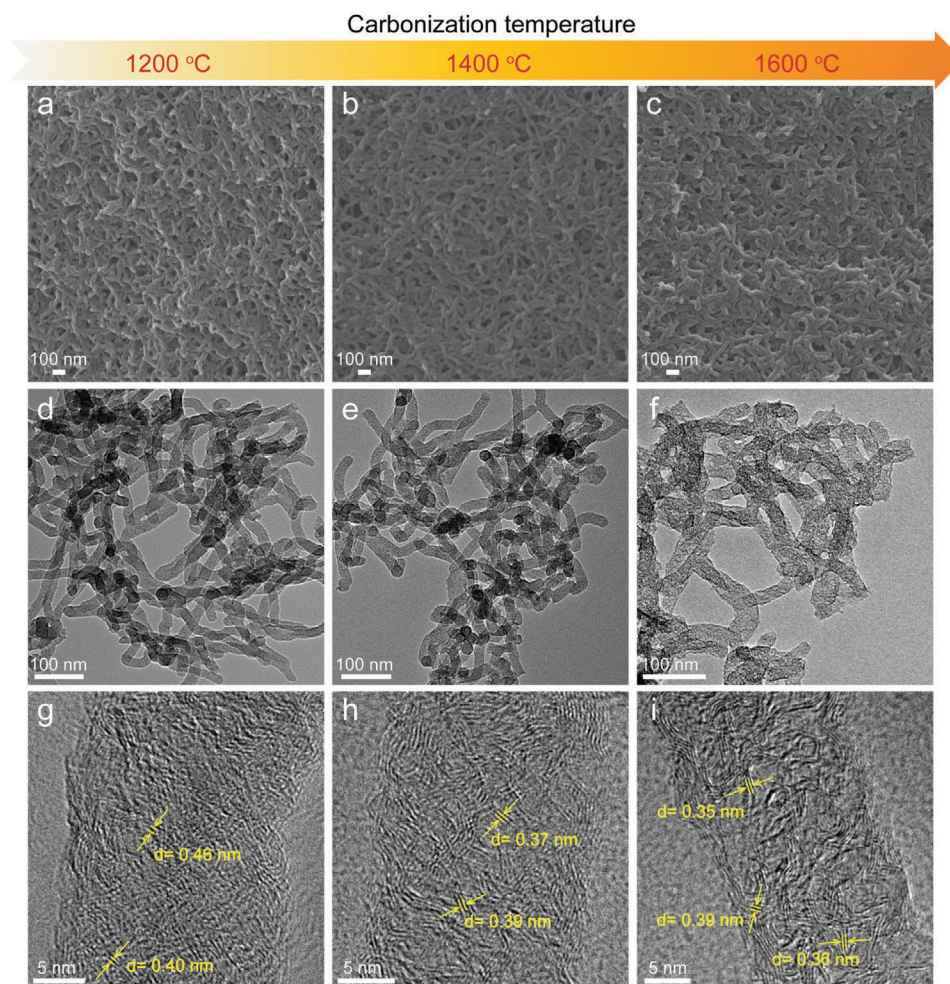


Figure 1. SEM a–c), TEM d–f), and HRTEM g–i) images of HCNF-1200, HCNF-1400, and HCNF-1600, respectively.

2. Results and Discussion

The synthesis of HCNFs is realized through phenol-aldehyde polymerization with subsequent carbonization.^[4] First, resin/cetyltrimethylammonium bromide (CTAB) composite fibers are synthesized via the polymerization of 3-aminophenol and formaldehyde in the presence of CTAB and ammonia in an aqueous solution. The CTAB acts as a structure directing agent, while the ammonia functions as a catalyst. Both ammonia and formaldehyde are derived from the hydrolysis of hexamethylenetetramine (HMTA). After carbonization, the resin/CTAB composite fibers can be successfully converted into HCNFs.

The morphological features of HCNFs are studied using scanning electron microscopy (SEM) and Transmission electron microscopy (TEM). HCNF-1200, HCNF-1400, and HCNF-1600 all exhibit a cross-linking nanofiber morphology (Figure 1a–c). The well-maintained nanofiber structure at an extremely high carbonization temperature of 1600 °C indicates the robustness of the HCNFs, and the high-temperature carbonization is beneficial to the increasing of graphitization degree and thus electrical conductivity of the product. The HCNFs possess a uniform diameter of about 20 nm and their lengths are in the range of 200 to 1000 nm (Figure 1d–f). The effects of annealing

temperature on the diameter and length of HCNFs are negligible. However, the surface of the HCNFs gradually roughs with the increase in carbonization temperature from 1200 to 1600 °C, which is caused by the graphitization of amorphous carbon (Figure S1 and S2, Supporting Information). High-resolution TEM (HRTEM) images of HCNF-1200, HCNF-1400, and HCNF-1600 (Figure 1g–i) reveal the detailed structural evolution process of HCNFs with the increasing of carbonization temperature. The HCNF-1200 presents scattered and highly disordered graphitic layers with large interlayer spacings, generally over 0.40 nm. The HCNF-1400 possesses abundant and defined few-layer stacked domains with interlayer spacings of 0.37–0.40 nm. The graphitic layers are orderly arranged in short range. However, for the HCNF-1600, the amount of short graphitic layers reduces while long-range arranged domains appear. The interlayer spacings become further narrow, approaching the spacings of graphite (0.34 nm), which are considered to be too narrow for sodium-ion intercalation.⁴

XRD patterns of the HCNF-1200, HCNF-1400, and HCNF-1600 are displayed in Figure 2a. All patterns present two broad peaks at ≈ 23 and 42° , representing the (002) and (100) planes of HC, respectively. With the rising of carbonization temperature, the diffraction peaks become sharper and the (002) peak gradually shifts

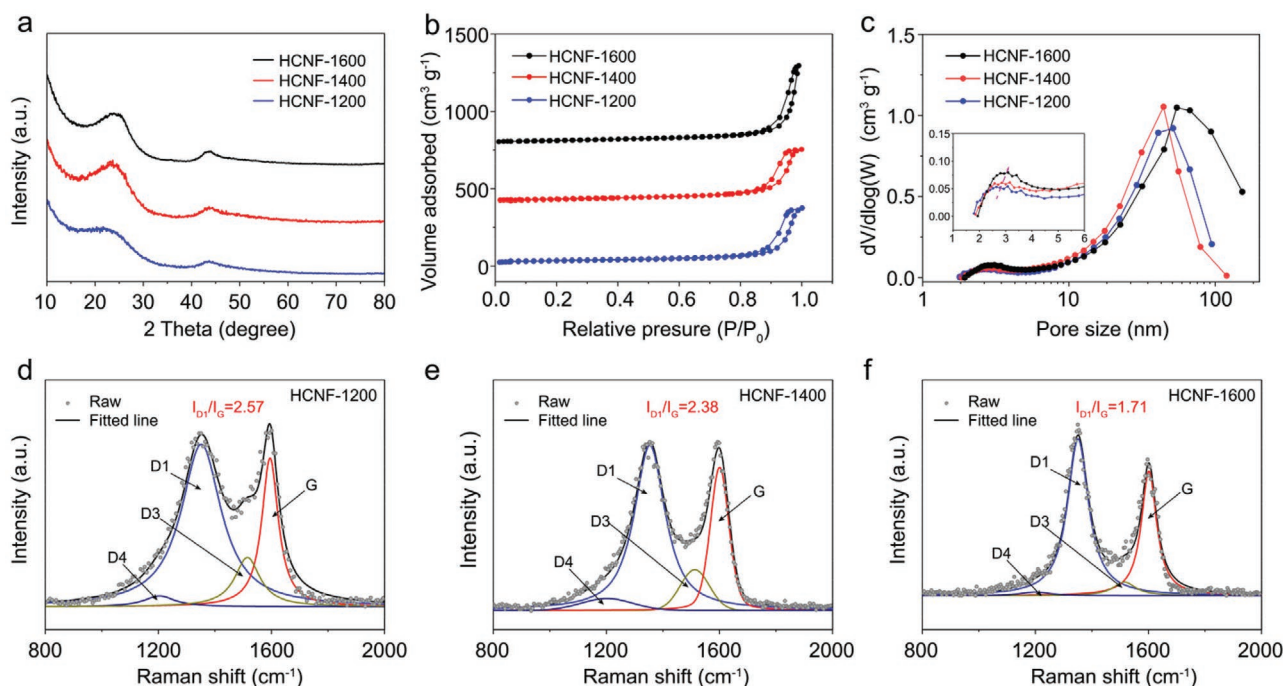


Figure 2. Structural characterizations of the HCNFs. a) XRD patterns, b) N_2 sorption isotherms, c) pore size distributions and the inset is the enlarged figure showing the small mesopores. Raman spectra of HCNF-1200 (d), HCNF-1400 (e) and HCNF-1600 (f).

to higher angles (Figure S3, Supporting Information), indicating the growth in crystalline domain size and reduction in interlayer distances, which agrees well with the HRTEM results.

XPS is conducted to detect the surface elemental contents and bonding configuration in HCNFs (Figure S4, Supporting Information). As shown in the survey spectra, there are three major elements (C, N, O) in the as-synthesized HCNF samples. The O and N contents show an inverse correlation with carbonization temperature. With the increase in carbonization temperature from 1200 to 1600 °C, the atomic ratio of O content decreases from 3.3 to 2.4 at.% and the N content decreases from 2.2 to 0.7 at.%. For carbon materials, the introduction of heteroatoms such as O and N is usually accompanied by the formation of defects. With the rising carbonization temperature, the defects will diminish gradually, and this deduction will be proved later through Raman spectroscopy. The C 1s spectra of all samples can be divided into three peaks located at 284.8, 286.5, and 285.7 eV, representing the C–C, C–O, and C–N bonds, respectively.

N_2 sorption results provide information on the surface area and pore size of the HCNFs. All samples manifest typical type IV isotherms with H1 hysteresis loops (Figure 2b), indicating the existence of mesopores.³⁶ The surface areas of HCNF-1200, HCNF-1400, and HCNF-1600 are 116, 98, and 108 $m^2 g^{-1}$, respectively. The N_2 adsorbed amount increases sharply at high relative pressures ($P/P_0 > 0.90$), suggesting the presence of large mesopores, which can also be reflected in the pore size distributions (Figure 2c). Actually, two kinds of mesopores can be noticed in the pore size distributions, small mesopores generally below 5 nm and large mesopores with a size of tens of nanometers. The small mesopores may be caused by the release of heteroatoms at high temperature, while the large mesopores are from the inter-particle voids of the intercon-

necting nanofibers. Such large mesopores are highly beneficial to electrolyte penetration and rate capability enhancement.

Raman spectra (Figure 2d–f) are employed to investigate the local structure of HCNFs. Each spectrum can be deconvoluted into four bands based on Lorentzian numerical simulation. The integral I_{D1}/I_G areal ratio decreases as the carbonization temperature rises, indicating the reduction of defects and the proceeding of graphitization.

Electrochemical performances of the HCNFs are studied in half-cells. The initial discharge/charge profiles of the HCNF samples at 30 $mA g^{-1}$ are displayed in Figure 3a. All the charge profiles present a slope region above 0.1 V and a plateau region below 0.1 V versus Na^+/Na , which are typical for HC materials. The initial Coulombic efficiency (ICE) of HCNFs can be calculated from the discharge/charge profiles. The HCNF-1400 demonstrates the highest ICE of 53%, substantially higher than those of HCNF-1200 (38%) and HCNF-1600 (30%). The first charge capacity as well as its slope-region and plateau-region contributions calculated from the initial charge profile are presented in Figure 3b. Among the three HCNF samples, the HCNF-1400 demonstrates the highest charge capacity of 388 $mAh g^{-1}$, while those of HCNF-1200 and HCNF-1600 are 238 and 205 $mAh g^{-1}$, respectively. With the increase in carbonization temperature, the slope-region capacity shows an obvious declining trend. As for the plateau-region capacity, its maximum value (201 $mAh g^{-1}$) is obtained at a carbonization temperature of 1400 °C and this value accounts for 52% of the total capacity of HCNF-1400. Further increase of the carbonization temperature causes a sharp decrease in plateau-region capacity.

The cycling performances of the HCNFs at 30 $mA g^{-1}$ are displayed in Figure 3c. The HCNF-1400 delivers a high second

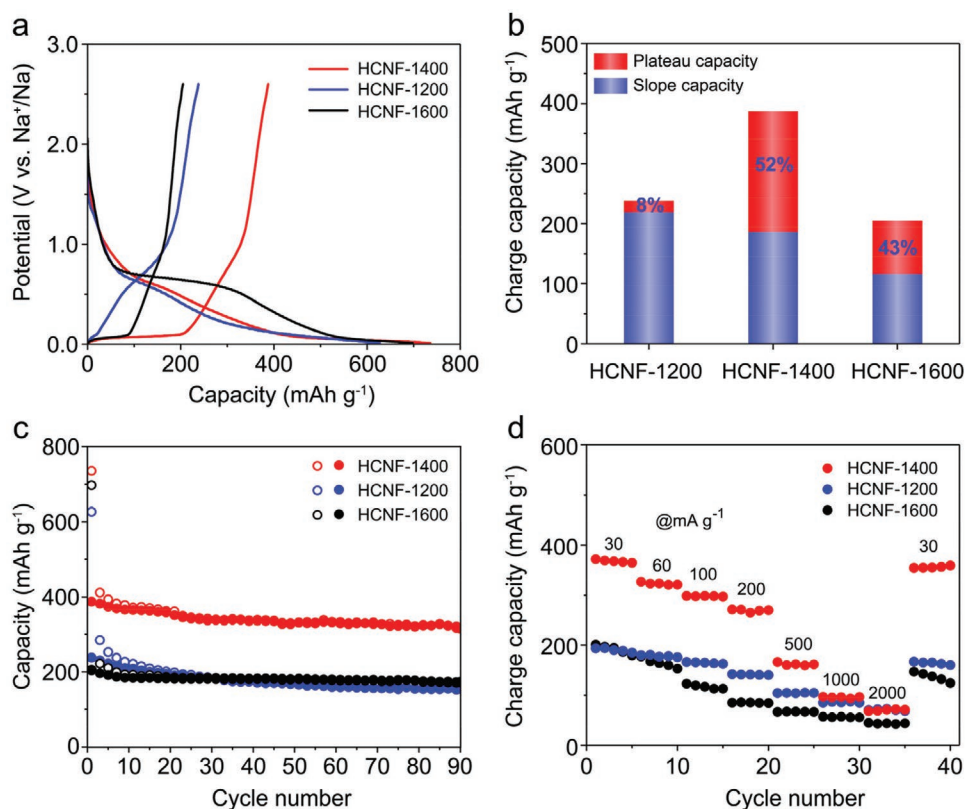


Figure 3. Sodium storage performances of the HCNFs. a) The first discharge/charge profiles, b) the contributions of slope-region capacity (>0.1 V) and plateau-region capacity (<0.1 V) in the first charge process, c) the cycling performances at 30 mA g^{-1} , and d) rate performances.

discharge capacity of 434 mAh g^{-1} and capacity retention of 82% over 90 cycles. Under the same conditions, the capacity retentions of HCNF-1200 and HCNF-1600 are 65% and 85%, respectively. The rate performances of HCNFs are provided in Figure 3d. The reversible capacities of HCNF-1400 are $372\text{--}69\text{ mAh g}^{-1}$ at $30\text{--}2000\text{ mA g}^{-1}$. With the decrease in current density, a capacity of 360 mAh g^{-1} can be recovered at 30 mA g^{-1} . At current densities over 500 mA g^{-1} , the plateau-region capacity diminishes sharply (Figure S5, Supporting Information), which is caused by the polarization and sluggish Na^+ diffusion. At 1 A g^{-1} , the HCNF-1400 exhibits good cycling stability with 0.017% capacity decay per cycle (Figure S6, Supporting Information).

The CV curves of HCNF-1400 (Figure S7, Supporting Information) show a pair of redox peaks at around 0.1 V, corresponding to the plateau region of the discharging/charging curves and the cathodic peak at about 0.5 V can be assigned to the forming of a solid electrolyte interface (SEI). EIS measurements are carried out to study the reaction kinetics (Figure S8, Supporting Information). The HCNF-1400 exhibits the lowest charge transfer resistance (R_{ct}) at the high-frequency region, indicating its fastest charge transfer on the electrode/electrolyte interface. It is noteworthy that the slope of the low-frequency line for HCNF-1400 is slightly lower than those of HCNF-1200 and HCNF-1600. This suggests that the Na^+ diffusion is more sluggish in HCNF-1400 as more graphitic layers exist.

Time-resolved in-situ Raman, which is sensitive to the evolution of crystal and local structures, is employed to investi-

gate the sodium storage mechanism of HCNF-1400. Previous studies indicate that the intercalation of Li^+/Na^+ in the graphitic layers of HC would cause the electron occupation in the π^* anti-bonding band, which weakens the C–C bond and elongates the bond length, thus leading to a redshift of the G-band. [39,42–44] The recorded in-situ Raman spectra with the corresponding initial discharge/charge curves are displayed in Figure 4a. Upon discharging in the slope region, the G-band gradually splits into two bands and shifts to lower wavenumbers, corresponding to the intercalation of Na^+ into the interlayers of graphitic carbon. At the plateau region, the G-band remains almost unchanged, indicating that the pore filling sodium storage is proceeding. The D-band decreases in intensity during sodiation, which may be caused by the Na^+ adsorption on the surfaces and various defects of the HCNFs.

Time-resolved in-situ XRD further effectively monitors the change in interlayer spacings (Figure 4b). Upon initial sodiation in the slope region, the broad (002) diffraction experiences obvious peak narrowing and intensity decreasing, suggesting the Na^+ ions are inserted into the interlayers and the generation of NaC_x compounds. It should be mentioned that the Na^+ insertion may be accompanied by Na^+ adsorption on the surface and defects, especially when considering the relatively high surface area of HCNFs and the capacitive contribution in the CV test (Figure S7d, Supporting Information). Upon deep sodiation in the plateau region, the (002) diffraction doesn't change obviously, indicating the pore filling mechanism. With subsequent charging, slight peak broadening can be noticed at the

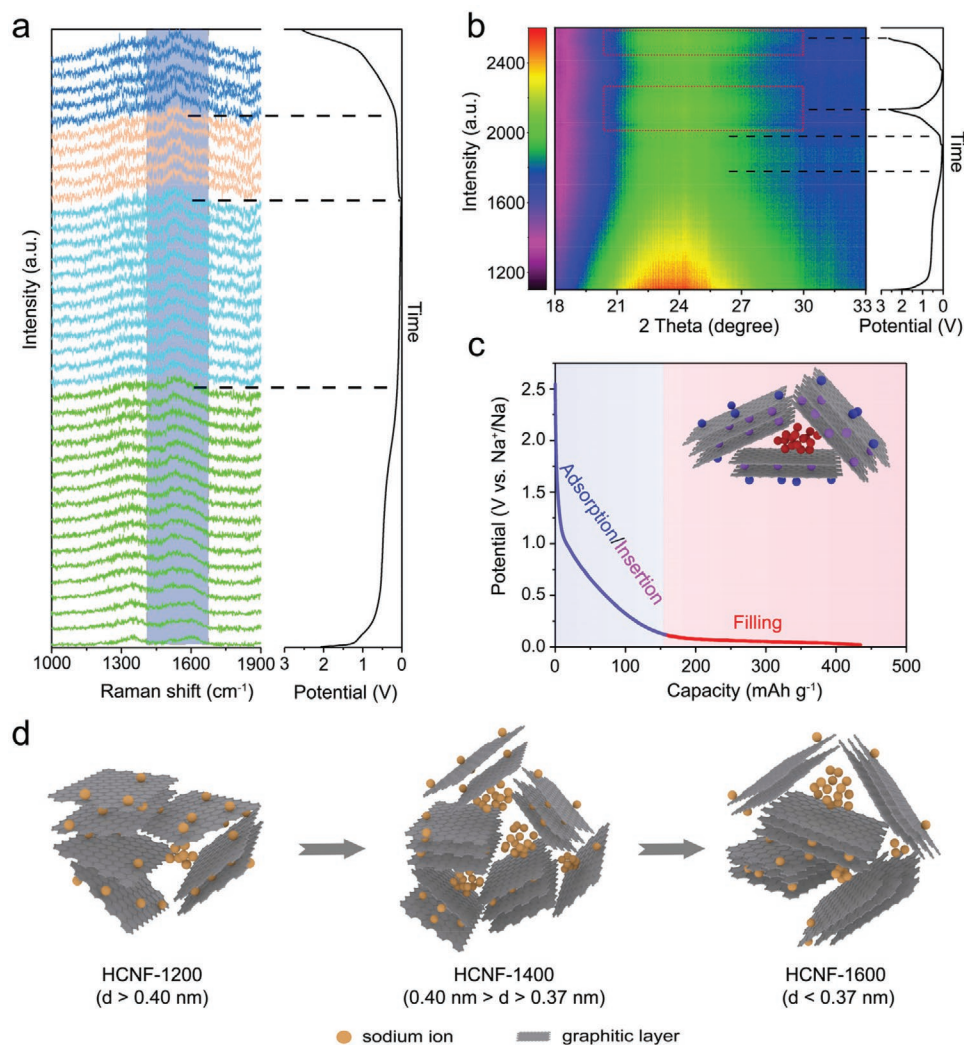


Figure 4. In-situ Raman spectra (a) and in-situ XRD patterns (b) of the HCNF-1400. c) Schematic illustration for the adsorption/insertion–filling sodium storage mechanism in the HCNFs. d) Schematic illustration for the sodium storage manners of HCNF-1200, HCNF-1400, and HCNF-1600.

end of charging. Such changes also occur in the second cycle, indicating the good reversibility. Generally, the information obtained from the in-situ XRD pattern is highly consistent with that obtained from the in-situ Raman characterization, further confirming an adsorption/insertion–filling sodium storage mechanism.

To further understand the Na⁺ insertion behavior in hard carbon, DFT calculation is performed to calculate the energy cost of Na⁺ insertion into carbon with interlayer distances of 3.4, 3.7, 4.0, and 4.5 Å (Figure 5a). When the interlayer distance is 3.4 Å (approximately the graphite), the energy cost is 0.906 eV, which is not feasible for Na⁺ insertion. But when the interlayer distance increased to 3.7 Å, the energy cost drastically decreased to −0.196 eV, suggesting the Na⁺ can be inserted into the interlayers. After further increasing the interlayer distance to over 4.0 Å, the energy cost is below −0.856 eV, indicating the Na⁺ can intercalate into the interlayers more easily.

Based on the above analyses, one can conclude that the Na⁺ adsorption on surfaces/defects and the Na⁺ insertion into interlayers occur simultaneously at the slope region. Once these

sites are occupied, the excess Na⁺ will be filled in the pores adjacent to the graphitic layers at the plateau region, and the interlayer spacings provide sufficient diffusion channels for Na⁺ to reach the pores. The sodium storage manners from HCNF-1200 to HCNF-1600 are schematically shown in Figure 4d. The graphitic interlayer spacing of HCNF-1200 is generally larger than 0.40 nm, which is large enough for the free diffusion of Na⁺. However, owing to the low carbonization temperature, the HCNF-1200 possesses relatively small amounts of graphitic domains for sodium-ion insertion and graphitic domain closed pores for sodium filling. As a result, the sodium ions are mainly adsorbed on the surfaces/defects in HCNF-1200, leading to low plateau-region capacity. In contrast, the HCNF-1400 provides not only sufficient interlayer spacing (0.37–0.40 nm) for Na⁺ intercalation but also abundant short-range graphitic domains with enclosed pores, thus leading to high slope-region and plateau-region capacities. As for the HCNF-1600, the interlayer spacings are too narrow for the efficient Na⁺ diffusion and intercalation, leading to the lowest slope capacity and the decreasing of Na⁺ to reach the pores, thus leading to

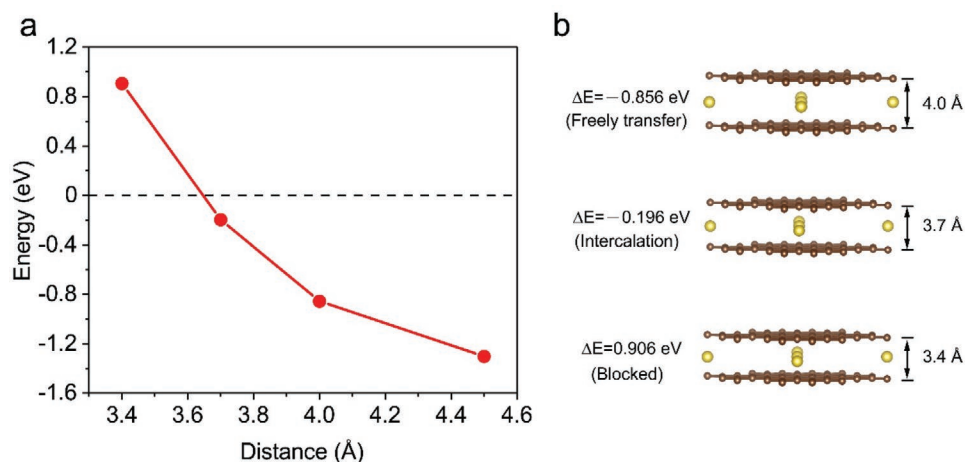


Figure 5. DFT calculation for Na⁺ insertion into hard carbon with different interlayer spacings. a) The calculated energy cost as a function of interlayer distance. b) The calculation models for the insertion of Na⁺ into hard carbon.

the decrease in plateau capacity. Considering the fact that the number of defects decreases with carbonization temperature, it is not surprising that the slope-region capacity that comes from Na⁺ adsorption/insertion also decreases with carbonization temperature (Figure 3b).

Galvanostatic intermittent titration technique (GITT) tests were employed to determine the apparent Na⁺ diffusion coefficient (D_{Na^+}) in HCNFs (Figure S9, Supporting Information). The D_{Na^+} is calculated based on the simplified equation. The average D_{Na^+} for HCNFs at the plateau region are obviously

lower than that at the slope region in both discharging and charging processes, indicating the Na⁺ diffusion is more sluggish at the plateau region. Considering this fact, it is quite reasonable that the plateau-region capacity decays more obviously at high current densities. HCNF-1200 exhibits a higher D_{Na^+} in the slope region than the HCNF-1400 and HCNF-1600, which can be ascribed to the larger interlayer spacings of HCNF-1200. The high D_{Na^+} enables HCNF-1200 to have good rate capacity. These results indicate that the construction of HC materials with appropriate graphitic interlayer spacings and abundant

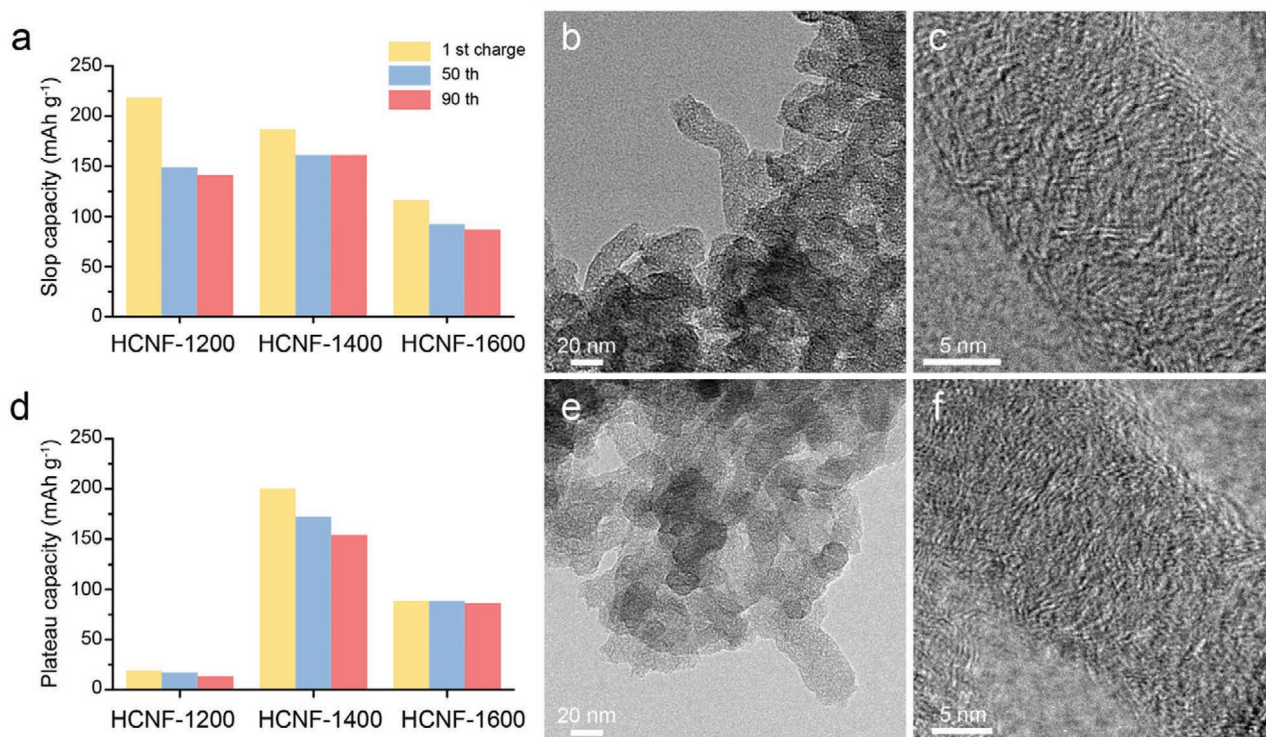


Figure 6. Slope-region (a) and plateau-region (d) capacities of the HCNFs at the 1st, 50th, and 90th cycles. TEM and HRTEM images of the HCNF-1400 after 50 cycles (b,c) and 90 cycles (e,f).

short-range graphitic domains with enclosed pores is an effective approach to achieving high-capacity and high-power sodium storage.

To reveal the reason for capacity degradation during cycling, the slope-region and plateau-region capacities of the HCNFs at 1st, 50th, and 90th cycles are presented in **Figure 6a,d**. The slope-region capacity decreases sharply in the first 50 cycles and then slows down in decay. The plateau-region capacity analogously decreases with cycling. Particularly, the HCNF-1400 exhibits a more obvious decay in plateau-region capacity than the HCNF-1200 and HCNF-1600. Ex-situ TEM images of the HCNF-1400 after 50 and 90 cycles are collected to investigate the structural integrity upon repeated Na⁺ insertion/extraction (**Figure 6b,c,e,f**). The HCNF-1400 can maintain the nanofiber morphology after repeated cycles, indicating the outstanding structural stability. HRTEM of the HCNF-1400 after 50 cycles still display clear few-layer stacked graphitic layers while the graphitic layers after 90 cycles are quite obscure and neat, which may be caused by the duplicated Na⁺ insertion/extraction induced destruction of short-range graphitic domains. Such change in microstructure is responsible for the decrease of plateau-region capacity.

3. Conclusions

In summary, a series of hard carbon nanofibers (HCNFs) with tunable interlayer spacings are successfully prepared by carbonizing resin nanofibers at different temperatures. Various characterizations are employed to monitor the texture evolution of the HCNFs with increasing carbonization temperature. With increasing carbonization temperature, the HCNFs gradually transform from disordered to ordered local structure accompanied by the generation of short-range graphitic domains and decreasing of defects. In addition, the interlayer spacing of the graphitic domains narrows with increasing carbonization temperature. In-situ XRD and Raman measurements reveal a revised adsorption/insertion–filling sodium storage mechanism. Combined with the DFT calculation, the detailed relationship between pore-filling plateau capacity and interlayer spacing is disclosed. The sufficient interlayer spacings (>0.37 nm) provide diffusion channels for Na⁺ to reach the pores for further filling. The optimized HCNF-1400 with abundant short-range graphitic domains and sufficient interlayer spacings (0.37–0.40 nm) for Na⁺ diffusion demonstrates high reversible sodium storage capacity (388 mAh g⁻¹ at 30 mA g⁻¹) and good rate performance (167 mAh g⁻¹ at 500 mA g⁻¹). In addition, the capacity degradation mechanism during cycling is disclosed. This study not only provides new insights into the sodium storage mechanism of hard carbon materials, but also affords a rational design strategy for high-performance hard carbon materials.

4. Experimental Section

Synthesis of HCNFs: In a typical synthesis, 0.4 g 3-aminophenol and 1.028 g HMTA were dissolved into 40 ml deionized water with stirring. After which, 0.3 g cetyltrimethylammonium bromide (CTAB) was added and stirred for 20 mins. The solution was heated to 85 °C and allowed to react

under static conditions for 24 h. The resulting resin/CTAB composite can be obtained after freeze-drying. After annealing the resin/CTAB composite at a certain temperature for 3 h in N₂, HCNFs can be obtained. The samples prepared at 1200, 1400, and 1600 °C are denoted as HCNF-1200, HCNF-1400, and HCNF-1600, respectively.

Materials Characterization: Scanning electron microscopy (SEM) images were collected on a JEOL-7100F microscope at 20 kV. Transmission electron microscopy (TEM) and high-resolution TEM (HRTEM) images were obtained on a JEOL JEM-2100F STEM/EDS microscope with the acceleration voltage of 200 kV. X-ray diffraction (XRD) was performed by a Bruker D8 Advance X-ray diffractometer with a Cu K α X-ray source ($\lambda = 1.5418 \text{ \AA}$). Raman spectra were recorded using a Horiba LabRAM HR Evolution with an excitation laser of 532 nm wavelength, the laser power was 2.61 mW and the diameter of the laser spot was 1.3 μm . The specific surface areas were calculated with the multipoint Brunauer–Emmett–Teller (BET) method using a Tristar II 3020 instrument by N₂ sorption at 77 K and pore size distributions (PSD) were obtained using a non-local density functional theory (NLDFT) model from the adsorption line of the isotherm. X-ray photoelectron spectroscopy (XPS) was carried out on a Thermo VG Multilab 2000 equipped with an Al K α monochromated X-ray source. The electrodes for In-situ XRD and Raman consisted of 90 wt.% of HCNF-1400 and 10 wt.% of polytetrafluoroethylene (PTFE). The HCNF-1400 based electrode was discharged to 0.01 V and then charged to 2.6 V at 50 mA g⁻¹. For the ex-situ measurements, the electrode was disassembled from the coin cell in an argon-filled glove box and washed in ethanol repeatedly followed by a drying process.

Electrochemical Characterization: The electrochemical performances were tested by assembling CR2016 coin cells in the Ar-filled glove box. Sodium foil was used as both the counter and reference electrodes. The electrode was prepared by casting the slurry containing 70 wt.% of HCNFs, 20 wt.% of acetylene black, and 10 wt.% of polyvinylidene fluoride in N-methyl-2-pyrrolidone onto copper foil and dried at 70 °C overnight. 1.0 M NaClO₄ in ethylene carbonate (EC) and dimethyl carbonate (DMC) (1:1 in volume) was used as the electrolyte and glass fiber was used as the separator. The mass loading of active materials was 1.2–1.5 mg cm⁻². Galvanostatic charge/discharge (GCD) measurements were performed with a multichannel battery testing system (LAND CT2001A) in the potential range of 0.01–2.6 V (vs. Na⁺/Na). Cyclic voltammetry (CV) and electrochemical impedance spectroscopy (EIS) were conducted on CHI600E and Autolab PGSTAT 302N electrochemical workstations, respectively.

Calculation Method: First-principle calculations were performed by the density functional theory (DFT) using the Vienna Ab-initio Simulation Package (VASP) package.^[45] The generalized gradient approximation (GGA) with the Perdew–Burke–Ernzerhof (PBE) functional was used to describe the electronic exchange and correlation effects.^[46–48] Uniform G-centered k-points meshes with only G point and Methfessel–Paxton electronic smearing were adopted for the integration in the Brillouin zone for geometric optimization. The simulation was run with a cutoff energy of 500 eV throughout the computations. These settings ensure convergence of the total energies to within 1 meV per atom. Structure relaxation proceeded until all forces on atoms were less than 1 meV \AA^{-1} and the total stress tensor was within 0.01 GPa of the target value. The structural model used in the DFT calculations was based on the reported model.^[43,49] The energy cost of Na inserted into carbon was calculated by the following equation: $\Delta E(\text{cost}) = [E(\text{total}) - E(\text{graphite}) - 2E(\text{Na})]/2$.

Supporting Information

Supporting Information is available from the Wiley Online Library or from the author.

Acknowledgements

C. C. and Y. C. contributed equally to this work. This work was supported by the National Natural Science Foundation of China (51832004), the

Shenzhen Fundamental Research Program (JCY20190809114409397), Sanya Science and Education Innovation Park of Wuhan University of Technology (2020KF0024), the Fundamental Research Funds for the Central Universities (WUT: 2020-YB-007, WUT: 2020-zy-012), Foshan Xianhu Laboratory of the Advanced Energy Science and Technology Guangdong Laboratory (XHT2020-003), the State Key Laboratory of Advanced Technology for Materials Synthesis and Processing (WUT: 2021-KF-7).

Conflict of Interest

The authors declare no conflict of interest.

Data Availability Statement

Research data are not shared.

Keywords

hard carbons, nanofibers, sodium storage mechanisms, slope capacity, plateau capacity

Received: September 1, 2021

Revised: October 16, 2021

Published online: December 2, 2021

- [1] C. Masquelier, L. Croguennec, *Chem. Rev.* **2013**, *113*, 6552.
- [2] Y. Huang, Y. Zheng, X. Li, F. Adams, W. Luo, Y. Huang, L. Hu, *ACS Energy Lett.* **2018**, *3*, 1604.
- [3] H. Kim, H. Kim, Z. Ding, M. H. Lee, K. Lim, G. Yoon, K. Kang, *Adv. Energy Mater.* **2016**, *6*, 1600943.
- [4] Y. Liu, B. V. Merinov, W. A. Goddard, *Proc. Natl. Acad. Sci. USA* **2016**, *113*, 3735.
- [5] B. Wang, E. H. Ang, Y. Yang, Y. Zhang, H. Geng, M. Ye, C. C. Li, *Adv. Funct. Mater.* **2020**, *30*, 2001708.
- [6] M. Hou, Y. Qiu, G. Yan, J. Wang, D. Zhan, X. Liu, J. Gao, L. Lai, *Nano Energy* **2019**, *62*, 299.
- [7] H. Liu, M. Jia, Q. Zhu, B. Cao, R. Chen, Y. Wang, F. Wu, B. Xu, *ACS Appl. Mater. Interfaces* **2016**, *8*, 26878.
- [8] P. Ge, X. Cao, H. Hou, S. Li, X. Ji, *ACS Appl. Mater. Interfaces* **2017**, *9*, 34979.
- [9] Y. Huang, X. Hu, J. Li, J. Zhang, D. Cai, B. Sa, H. Zhan, Z. Wen, *Energy Storage Mater.* **2020**, *29*, 121.
- [10] H. Xie, W. P. Kalisvaart, B. C. Olsen, E. J. Luber, D. Mitlin, J. M. Buriak, *J. Mater. Chem. A* **2017**, *5*, 9661.
- [11] X. Dou, I. Hasa, D. Saurel, C. Vaalma, L. Wu, D. Buchholz, D. Bresser, S. Komaba, S. Passerini, *Mater. Today* **2019**, *23*, 87.
- [12] H. Hou, X. Qiu, W. Wei, Y. Zhang, X. Ji, *Adv. Energy Mater.* **2017**, *7*, 1602898.
- [13] S. Alvin, H. S. Cahyadi, J. Hwang, W. Chang, S. K. Kwak, J. Kim, *Adv. Energy Mater.* **2020**, *10*, 2000283.
- [14] T. Zhang, L. Yang, X. Yan, X. Ding, *Small* **2018**, *14*, 1802444.
- [15] Y. Li, S. Xu, X. Wu, J. Yu, Y. Wang, Y.-S. Hu, H. Li, L. Chen, X. Huang, *J. Mater. Chem. A* **2015**, *3*, 71.
- [16] F. Shen, W. Luo, J. Dai, Y. Yao, M. Zhu, E. Hitz, Y. Tang, Y. Chen, V. L. Sprenkle, X. Li, L. Hu, *Adv. Energy Mater.* **2016**, *6*, 1600377.
- [17] Q. Wang, X. Zhu, Y. Liu, Y. Fang, X. Zhou, J. Bao, *Carbon* **2018**, *127*, 658.
- [18] H. Wang, W. Yu, J. Shi, N. Mao, S. Chen, W. Liu, *Electrochim. Acta* **2016**, *188*, 103.
- [19] Y. Zhu, M. Chen, Q. Li, C. Yuan, C. Wang, *Carbon* **2018**, *129*, 695.
- [20] S. Y. Cho, M. Kang, J. Choi, M. E. Lee, H. J. Yoon, H. J. Kim, C. Leal, S. Lee, H. J. Jin, Y. S. Yun, *Small* **2018**, *14*, 1703043.
- [21] X. Hu, X. Sun, S. J. Yoo, B. Evanko, F. Fan, S. Cai, C. Zheng, W. Hu, G. D. Stucky, *Nano Energy* **2019**, *56*, 828.
- [22] H. Liu, M. Jia, N. Sun, B. Cao, R. Chen, Q. Zhu, F. Wu, N. Qiao, B. Xu, *ACS Appl. Mater. Interfaces* **2015**, *7*, 27124.
- [23] X. Lin, Y. Liu, H. Tan, B. Zhang, *Carbon* **2020**, *157*, 316.
- [24] X. Li, Z. Liu, C. Cai, Q. Yu, W. Jin, M. Xu, C. Yu, S. Li, L. Zhou, L. Mai, *ChemSusChem* **2021**, *14*, 1756.
- [25] J. L. Xia, D. Yan, L. P. Guo, X. L. Dong, W. C. Li, A. H. Lu, *Adv. Mater.* **2020**, *32*, 2000447.
- [26] J. Zhu, C. Chen, Y. Lu, Y. Ge, H. Jiang, K. Fu, X. Zhang, *Carbon* **2015**, *94*, 189.
- [27] Q. Jin, K. Wang, P. Feng, Z. Zhang, S. Cheng, K. Jiang, *Energy Storage Mater.* **2020**, *27*, 43.
- [28] Y. Qiao, J. Wu, X. Cheng, Y. Pang, Z. Lu, X. Lou, Q. Li, J. Zhao, S. Yang, Y. Liu, *J. Energy Chem.* **2020**, *48*, 435.
- [29] Y. Li, Y. Lu, Q. Meng, A. C. S. Jensen, Q. Zhang, Q. Zhang, Y. Tong, Y. Qi, L. Gu, M. M. Titirici, Y. S. Hu, *Adv. Energy Mater.* **2019**, *9*, 1902852.
- [30] Q. Meng, Y. Lu, F. Ding, Q. Zhang, L. Chen, Y.-S. Hu, *ACS Energy Lett.* **2019**, *4*, 2608.
- [31] Y. Xie, Y. Chen, L. Liu, P. Tao, M. Fan, N. Xu, X. Shen, C. Yan, *Adv. Mater.* **2017**, *29*, 1702268.
- [32] Z. Hong, Y. Zhen, Y. Ruan, M. Kang, K. Zhou, J. M. Zhang, Z. Huang, M. Wei, *Adv. Mater.* **2018**, *30*, 1802035.
- [33] Y. Qiao, R. Han, Y. Pang, Z. Lu, J. Zhao, X. Cheng, H. Zhang, Z. Yang, S. Yang, Y. Liu, *J. Mater. Chem. A* **2019**, *7*, 11400.
- [34] N. Fu, Y. Liu, R. Liu, X. Wang, Z. Yang, *Small* **2020**, *16*, 2001607.
- [35] Y. Liu, Y. Qiao, G. Wei, S. Li, Z. Lu, X. Wang, X. Lou, *Energy Storage Mater.* **2018**, *11*, 274.
- [36] S. Qiu, L. Xiao, M. L. Sushko, K. S. Han, Y. Shao, M. Yan, X. Liang, L. Mai, J. Feng, Y. Cao, X. Ai, H. Yang, J. Liu, *Adv. Energy Mater.* **2017**, *7*, 1700403.
- [37] N. Sun, Z. Guan, Y. Liu, Y. Cao, Q. Zhu, H. Liu, Z. Wang, P. Zhang, B. Xu, *Adv. Energy Mater.* **2019**, *9*, 1901351.
- [38] Y. Cao, L. Xiao, M. L. Sushko, W. Wang, B. Schwenzer, J. Xiao, Z. Nie, L. V. Saraf, Z. Yang, J. Liu, *Nano Lett.* **2012**, *12*, 3783.
- [39] D.-S. Bin, Y. Li, Y.-G. Sun, S.-Y. Duan, Y. Lu, J. Ma, A.-M. Cao, Y.-S. Hu, L.-J. Wan, *Adv. Energy Mater.* **2018**, *8*, 1800855.
- [40] L. Xiao, H. Lu, Y. Fang, M. L. Sushko, Y. Cao, X. Ai, H. Yang, J. Liu, *Adv. Energy Mater.* **2018**, *8*, 1703238.
- [41] Q. Yu, J. Lv, Z. Liu, M. Xu, W. Yang, K. A. Owusu, L. Mai, D. Zhao, L. Zhou, *Sci. Bull.* **2019**, *64*, 1617.
- [42] L. J. Hardwick, P. W. Ruch, M. Hahn, W. Scheifele, R. Kötz, P. Novák, *J. Phys. Chem. Solids* **2008**, *69*, 1232.
- [43] H. Euchner, B. P. Vinayan, M. A. Reddy, M. Fichtner, A. Groß, *J. Mater. Chem. A* **2020**, *8*, 14205.
- [44] M. Inaba, H. Yoshida, Z. Ogumi, *J. Electrochem. Soc.* **1996**, *143*, 2572.
- [45] G. Kresse, J. Furthüller, *Comput. Mater. Sci* **1996**, *6*, 15.
- [46] J. P. Perdew, K. Burke, M. Ernzerhof, *Phys. Rev. Lett.* **1996**, *77*, 3865.
- [47] P. E. Blöchl, *Phys. Rev. B: Condens. Matter Mater. Phys.* **1994**, *50*, 17953.
- [48] G. Kresse, D. Joubert, *Phys. Rev. B: Condens. Matter Mater. Phys.* **1999**, *59*, 1758.
- [49] M. Anji Reddy, M. Helen, A. Groß, M. Fichtner, H. Euchner, *ACS Energy Lett.* **2018**, *3*, 2851.